RSC Advances

PAPER

View Article Online
View Journal | View Issue

Cite this: *RSC Adv.*, 2017, **7**, 42774

Rational fabrication of a graphitic-C_3N_4/$Sr_2KNb_5O_{15}$ nanorod composite with enhanced visible-light photoactivity for degradation of methylene blue and hydrogen production†

Ping Wang, *[ab] Ilya Sinev,[c] Feng Sun,[a] Huijun Li,[a] Ding Wang,[a] Qian Li,[d] XianYing Wang,[a] Roland Marschall[be] and Michael Wark*[bf]

A g-C_3N_4/$Sr_2KNb_5O_{15}$ nanorod composite photocatalyst was simply prepared by direct growth of graphitic C_3N_4 on one-dimensional $Sr_2KNb_5O_{15}$ nanorods and evaluated by degradation of methylene blue (MB) and water splitting for H_2 production under visible light irradiation. By coupling g-C_3N_4 and $Sr_2KNb_5O_{15}$ nanorods, the nanocomposite with an optimal 77 wt% g-C_3N_4 exhibited 6.2 times higher activity for photodegradation than the bare g-C_3N_4 and the increase in H_2 production rate from an aqueous methanolic solution reached up to 12.1 fold after appropriate photodeposition of 0.03 wt% Rh cocatalysts. Furthermore, a comparative study on the preparation methods shows the photodegradation rate of the nanocomposite prepared by the direct growth method was found to be 3.4 times higher than those formed just by physical mixing. The results demonstrate the importance of the formation of proper nano-interfaces in the nanocomposite. Combined with theoretical prediction of the band structures, a possible mechanism is thus proposed including the formation of proper interfaces between g-C_3N_4 and $Sr_2KNb_5O_{15}$ by direct growth approachs promoting spatial separation of photoinduced electron–hole pairs.

Received 6th July 2017
Accepted 31st August 2017

DOI: 10.1039/c7ra07441g

rsc.li/rsc-advances

1. Introduction

The search for efficient heterogeneous photocatalysts has attracted considerable interest over the past decades due to their potential applications in environmental clean-up and solar energy conversion.[1–3] Among the various semiconductor-based photocatalytic materials, titania (TiO_2) is recognized as the most promising candidate for eliminating organic pollutants because of its low cost, high abundance in the Earth's crust, nontoxicity, and chemical stability.[4,5] However, the low quantum efficiency of TiO_2 photocatalysts, due to the absorption of only ultraviolet (UV) light (band gap of ~3.2 eV), and fast recombination of photogenerated electron–hole pairs limits their practical application.

In recent years, doping of metal cations (W, V, Fe, and Cr, *etc.*)[6–8] or nonmetal anions (C, N, B, S and F, *etc.*)[9–13] was extensively researched in order to develop visible light-driven photocatalysts, but unfortunately it usually gives rise to accelerated charge recombination, and interruption of the surface structures.[14,15] In order to boost solar energy efficiency, dye-sensitized solar cells have also been explored to enhance the light absorption in the visible region.[16,17] Currently among all the strategies delicate construction of hetero- or homo-junction semiconductor photocatalyst composite structures is thought to be the most promising approach for extending light absorption and improving charge separation.[18–20] Up to now, several semiconductor couples have been demonstrated to efficiently promote charge separation by the interfaces between the combined semiconductors, especially employing TiO_2 as one part.[21–27]

As a metal-free semiconductor, polymeric graphitic carbon nitride (g-C_3N_4), firstly reported by Wang *et al.* in 2009; it can enable both half reactions of water splitting in the presence of sacrificial reagents under visible light irradiation.[28,29] The small

[a]*School of Materials Science and Technology, University of Shanghai for Science and Technology, Jungong Road 516, Shanghai, 200093, P. R. China. E-mail: ping.wang@usst.edu.cn*

[b]*Laboratory of Industrial Chemistry, Ruhr-University Bochum, Universitaetsstrasse 150, 44801 Bochum, Germany*

[c]*Department of Physics, Ruhr-University Bochum, Universitaetsstrasse 150, 44801 Bochum, Germany*

[d]*Materials Genome Institute, Shanghai University, Shangda Road 99, 200444 Shanghai, P. R. China*

[e]*Institute of Physical Chemistry, Justus-Liebig-University Giessen, Heinrich-Buff-Ring 58, 35392 Giessen, Germany*

[f]*Institute for Chemistry, Chemical Technology 1, Carl von Ossietzky University Oldenburg, Carl-von-Ossietzky-Str. 9-11, 26129 Oldenburg, Germany. E-mail: michael.wark@uni-oldenburg.de*

† Electronic supplementary information (ESI) available: The crystallographic structure, TG curves, XPS data, TEM images, UV-Vis spectra, first-order kinetics model, recycle measurements and PL spectra. See DOI: 10.1039/c7ra07441g

band gap (*ca.* 2.70 eV) capable of visible light absorption, a quite negative conduction band minimum (−1.12 eV *vs.* NHE) and the high thermal and chemical stability render g-C_3N_4 as one of the most promising candidates for the fabrication of heterostructured composites.[30] By coupling of g-C_3N_4 with another narrow band-gap semiconductor, such as N–TiO_2,[31] N–$H_2Ta_2O_6$,[32] N–In_2TiO_5,[33] TaON,[34] $BiPO_4$,[35] Bi_2WO_6,[36] and α-Fe_2O_3,[37] *etc.*, the formation of heterojunctions has been demonstrated to promote the separation of photogenerated charge carriers thus improving the photocatalytic efficiency.[38,39] On the other hand, owing to the delocalized π-electrons from the conjugated π system of g-C_3N_4,[40] the combination of g-C_3N_4 with wide band gap semiconductors has been also developed. Successful examples include TiO_2,[41,42] ZnO,[43] titanate,[14,44] and Zn_2GeO_4.[45] In the previous work,[46] we have reported that the tetragonal tungsten bronze-type Ta substituted $Sr_2KNb_5O_{15}$ nanorod photocatalysts possess a unique tunnel structure with a built-in electric field along [001] direction and exhibit relatively high activity for photocatalytic water splitting under UV irradiation. The $Sr_2KNb_5O_{15}$ with a minimum band gap of ~3.2 eV shows a great potential as an alternative photocatalyst to TiO_2. However, the challenge in photocatalytic efficiency still remains and more efficient photocatalytic structures need to be developed.[19]

Inspired by this, here we report, for the first time, a g-C_3N_4/$Sr_2KNb_5O_{15}$ nanocomposite photocatalyst simply prepared by direct growth of g-C_3N_4 on $Sr_2KNb_5O_{15}$ nanorods. Under visible-light irradiation, the photocatalytic properties were significantly enhanced by coupling of g-C_3N_4 with $Sr_2KNb_5O_{15}$ for the degradation of methylene blue (MB) and photocatalytic hydrogen production. The highest photocatalytic activity was observed in the g-C_3N_4/$Sr_2KNb_5O_{15}$ nanocomposite with optimum g-C_3N_4 content of 77 wt%. The proposed mechanism was associated with the role of g-C_3N_4 as a visible light absorber unit, and the function of the inner $Sr_2KNb_5O_{15}$ nanorods as an electron separator, which is capable of adopting photoinduced electrons from the g-C_3N_4, *i.e.* the photoinduced electrons from the conduction band of g-C_3N_4 are injected into the $Sr_2KNb_5O_{15}$, while the photoinduced holes remain in the g-C_3N_4, thus promoting spatial separation of photoinduced electron–hole pairs. Furthermore, the study of Rh metal as co-catalysts for improving photocatalytic H_2 production points out that in the composite materials system the proper use of noble metal co-catalysts is an important issue. The resulting inhibition effect at high dosage of Rh may produce, affecting the interfacial charge transfer between g-C_3N_4 and $Sr_2KNb_5O_{15}$.

2. Experimental

Synthesis of photocatalysts

All reagents used in this study were used without further purification. The $Sr_2KNb_5O_{15}$ nanorods were prepared by molten salt method, as reported in our previous work.[46] Stoichiometric amounts of precursors $SrCO_3$ (>99.99%, Aldrich), K_2CO_3 (>99.9%, Alfa Aesar) and Nb_2O_5 (99.99%, Alfa Aesar) with potassium chloride (KCl: 99.5%, Honeywell Riedel-de Haën) at a weight ratio of 1 : 2 were heated at 850 °C in air for 2 h. The g-C_3N_4 was prepared by directly heating melamine ($C_3H_6N_6$, Alfa Aesar, >99%) to 520 °C for 4 h.[47] The direct growth method was used for preparation of g-C_3N_4/$Sr_2KNb_5O_{15}$ nanocomposite photocatalysts. Briefly, an appropriate weight ratio of melamine and $Sr_2KNb_5O_{15}$ was added into ethanol. The bottle was placed in an ultrasonic bath for 30 min for complete dispersion and then stirred in a fume hood. After drying at 80 °C overnight, the resultant mixture was heated to 520 °C in a covered porcelain crucible for 4 h. According to this method, different weight ratios of g-C_3N_4/$Sr_2KNb_5O_{15}$ samples with g-C_3N_4 contents of 24 wt%, 55 wt%, 77 wt% and 99 wt% were synthesized, and denoted as 24CNNb, 55CNNb, 77CNNb and 99CNNb, respectively. For comparison, a physical mixture of the pre-synthesized g-C_3N_4 and $Sr_2KNb_5O_{15}$ was also prepared without heat treatment (denoted as M77CNNb).

Characterization

The X-ray diffraction patterns of all samples were recorded with a PANalytical MPD diffractometer using Cu-Kα radiation (λ = 0.1541 nm), and the data were collected from 10° to 60° (2θ). Static N_2 physisorption measurements were carried out at −196 °C using a Quantachrome Autosorb-1MP system. All samples were degassed at 200 °C for 6 h before the measurements. Thermogravimetric analyses were conducted with a TG/DSC NETZSCH STA 409 PC instrument from room temperature to 1000 °C at a heating rate of 5 °C min^{-1} under nitrogen flow of 300 mL min^{-1}. UV-Vis diffuse reflectance spectra were measured using MgO as a reference on a Cary 4000 UV/Vis Varian spectrophotometer. Band gap energies were calculated by analysis of the Tauc-plots resulting from Kubelka–Munk transformation of diffuse reflectance spectra. The transmission electron microscopy and high-resolution transmission electron microscopy characterization of the materials were carried out using a Philips/FEI Tecnai F20 S-TWIN electron microscopy instrument operating at 200 kV. X-ray photoelectron spectroscopy (XPS) measurements were carried out in an ultra-high vacuum (UHV) set-up equipped with a monochromatic Al Kα X-ray source ($h\nu$ = 1486.6 eV), operated at 14.5 kV and 35 mA, and a high resolution Gammadata-Scienta SES 2002 analyzer. The base pressure in the measurement chamber was maintained at about 5×10^{-10} mbar. The measurements were carried out in the fixed transmission mode with pass energy of 200 eV resulting in an overall energy resolution of 0.25 eV. A flood gun was applied to compensate the charging effects. The Casa XPS software with a Gaussian–Lorentzian product function and Shirley background subtraction was used for peak deconvolution. To obtain a stable fit, single contributions of N 1s and C 1s signal deconvolution were constrained to have their full width at half maximum (FWHM) within the same range. The photoluminescence (PL) spectra were recorded at room temperature by using a Horiba LabRam HR spectrometer with the 325 nm line of He–Cd laser as excitation source.

Photocatalytic evaluation

Photodegradation of methylene blue. Methylene blue (MB) was adopted as the typically tested hazardous organic model

pollutant to evaluate the photocatalytic performance of as-prepared samples. The photocatalytic reaction system consisted of a 300 W Xe arc lamp as a light source (Newport Corporation), a GG400 filter (providing the visible light of different wavelength, >400 nm) and a Schott KG3 IR filter (preventing from thermal catalytic effect). All experiments were conducted at room temperature in air. In a typical run, 50 mg of catalysts was added into 100 mL of 10.0 mg L^{-1} MB solution. Prior to irradiation, the suspension was magnetically stirred in the dark for 40 min to ensure the adsorption–desorption equilibrium of MB on the surface of the photocatalyst. Under irradiation approximately 4 mL suspension was collected at given time intervals and separated through a syringe driven filter unit (Millex, Millipore Corp., USA). The concentration change of MB was detected by measuring its characteristic absorption peak at 665 nm on a Cary 4000 UV/Vis Varian spectrophotometer, a Perkin-Elmer Lambda 650 UV-Vis spectrometer was employed during the recovery experiments.

Photocatalytic H_2 production. The photocatalytic H_2 production was conducted in an air-tight reactor and a 500 W mid-pressure Hg arc lamp equipped with a cooling water filter at 15 °C and a 420 nm cut-off filter was used as a visible light irradiation source. The evolved H_2 was determined by gas chromatography (GC7900, Techcomp Ltd., Beijing, China) equipped with a MS-5A column and a thermal conductivity detector. High-purity N_2 (N_2, 5.0 quality) was used as carrier. In a typical run, 30 mg of the powders were added in 30 mL of 10 vol% aqueous methanolic solution and then dispersed by ultrasonication for 10 min. The Rh metal was stepwise deposited by *in situ* photoreduction using hexachlororhodate(III) (Na_3RhCl_6, Sigma Aldrich). Prior to irradiation, the whole system was purged with high-purity N_2 to remove air completely.

3. Results and discussion

Physicochemical properties

Estimation of the g-C_3N_4 content in the g-C_3N_4/$Sr_2KNb_5O_{15}$ composite samples was carried out by thermogravimetric analysis (TG, see Fig. S1†). The g-C_3N_4 content in the composite samples was more or less the same as the corresponding values calculated from balance measurement (see Table 1), and all TG weight losses had similar profiles within the experimental error.

Table 1 Physicochemical characterization of g-C_3N_4/$Sr_2KNb_5O_{15}$ nanocomposite samples

Sample	C_3N_4[a] (wt%)	S_{BET}[b] (m^2 g^{-1})	E_g[c] (eV)
$Sr_2KNb_5O_{15}$	0	19.1	3.21
24CNNb	30%	17.1	3.22/2.64
55CNNb	54%	19.6	2.66
77CNNb	80%	14.6	2.66
99CNNb	98%	13.2	2.65
g-C_3N_4	100%	11.2	2.66

[a] Estimated by TG. [b] Measured by the BET method. [c] Determined from the extrapolated straight line portion of the Tauc plot at $(F(R)\ h\nu)^{1/2} = 0$ (see Fig. 3 below).

For example, the content of g-C_3N_4 in the 77CNNb sample can be calculated to be approximately 80 wt% from the TG curve. The slight weight loss being observed before 300 °C corresponded to desorption of water. The major weight loss started at about 540 °C, and finished at about 730 °C, which can be attributed to the decomposition of g-C_3N_4. After 730 °C, no significant mass change was observed and accordingly the mass residue of the $Sr_2KNb_5O_{15}$ material can be determined. Moreover, the exposed surface areas of these nanocomposite samples were determined by the Brunauer–Emmett–Teller (BET) method from nitrogen adsorption–desorption measurements. As shown in Table 1, a slight decrease was observed in the g-C_3N_4/$Sr_2KNb_5O_{15}$ composite samples with g-C_3N_4 content higher than 55 wt%, probably due to the influence of constituent g-C_3N_4 with relative low BET surface area.

Crystal structure

The X-ray powder diffraction (XRD) patterns of the g-C_3N_4/$Sr_2KNb_5O_{15}$ nanocomposite samples with different content of g-C_3N_4 are shown in Fig. 1. The samples were well-crystallized and no significant peak shift can be observed. Fig. S2† illustrates in a schematic diagram the crystal structures of $Sr_2KNb_5O_{15}$ and g-C_3N_4. The bare $Sr_2KNb_5O_{15}$ can be indexed to tetragonal tungsten bronze structure (JCPDS No. 34-0108), which consists of a framework of corner-shared NbO_6 octahedral and three cationic tunnels A1, A2, and A3 along [001] direction (A1 and A2 sites are partially occupied by Sr and K atom and partially vacant, and A3 sites are vacant). The XRD pattern of bare g-C_3N_4 shows two distinct peaks at 13.2° and 27.4°, which can be indexed as the (100) and (002) diffraction planes, respectively, showing the construction of graphitic planes from tri-*s*-triazine

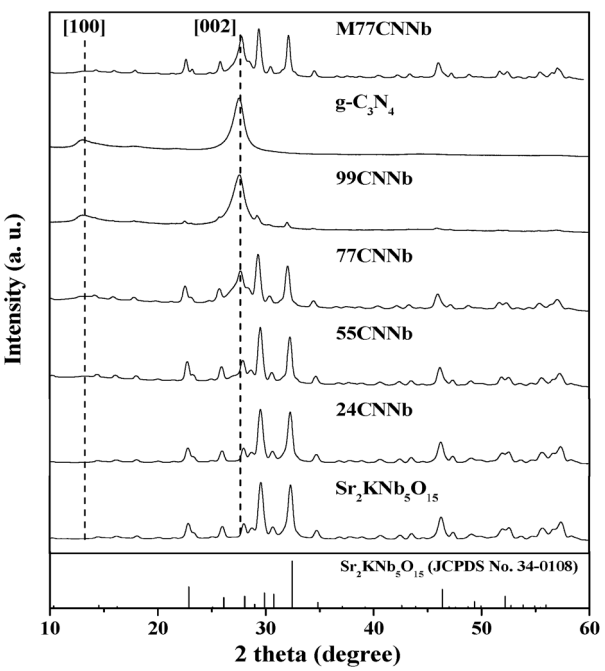

Fig. 1 XRD patterns of the g-C_3N_4/$Sr_2KNb_5O_{15}$ nanocomposite samples.

units were connected by planar amino groups.[48] The small-angle diffraction peak at 13.2° gives evidence to the (100) interplanar structural packing of tri-triazine units. The strong peak at 27.4° is the characteristic (002) interplanar stacking peak, corresponding to the interlayer distance of aromatic systems. The results indicate the formation of well-built g-C_3N_4 layer structure, in good agreement with the literature.[15] For the g-C_3N_4/$Sr_2KNb_5O_{15}$ nanocomposite samples, it was hard to differentiate the overlapping diffraction peaks of g-C_3N_4 at 27.4° and $Sr_2KNb_5O_{15}$ at 27.7° as long as the content of g-C_3N_4 was lower than 55 wt%. With the increased content of g-C_3N_4, the stronger intensity of the diffraction peak appearing at around 27.5° in the 77CNNb and 99CNNb samples mostly result from their superimposition effects. As shown in Fig. 1, similar XRD patterns were observed for the nanocomposite samples being prepared by direct growth (77CNNb) or by physically mixing (M77CNNb). In both cases no structural interaction between g-C_3N_4 and $Sr_2KNb_5O_{15}$ is observed.

Microstructure

Fig. 2 shows the representative transmission electron microscopy (TEM) images of bare $Sr_2KNb_5O_{15}$ (a), bare g-C_3N_4 (b), 77CNNb nanocomposite (c), and the high resolution transmission electron microscopy (HRTEM) image of 77CNNb nanocomposite (d), respectively. The bare $Sr_2KNb_5O_{15}$ sample exhibited nanorod morphology with diameters in the range of 100–400 nm (Fig. 2a) and lengths up to a few microns (Fig. 2b), while the bare C_3N_4 particles are irregular aggregated. As compared with bare $Sr_2KNb_5O_{15}$ and g-C_3N_4, it can be clearly seen (Fig. 2c) that most of the $Sr_2KNb_5O_{15}$ nanorod surfaces were intimately surrounded by g-C_3N_4 in the nanocomposite with high g-C_3N_4 content (77CNNb), indicating that this coverage might favor the formation of sufficient interfaces. In order to further examine the structure, HRTEM analysis was employed. The HRTEM images of the 77CNNb nanocomposite (Fig. 2d and S3†) confirm the expected interplanar spacing of 0.32 nm of the [211] crystal planes of $Sr_2KNb_5O_{15}$ as well as the coverage of the $Sr_2KNb_5O_{15}$ nanorod by g-C_3N_4. Presumably, the photo-induced charge transfer *via* the interfaces was spatially smooth which was fundamental for improving the photocatalytic activity, as will be discussed in detail below.

Optical property

Fig. 3 shows Kubelka–Munk transformed UV-Vis diffuse reflection spectra (DRS) and Tauc plots (inset) of the g-C_3N_4/$Sr_2KNb_5O_{15}$ nanocomposites. The band gaps of bare $Sr_2KNb_5O_{15}$ and g-C_3N_4 can be estimated to be about 3.21 eV and 2.66 eV, respectively. A shoulder in the absorption was clearly observed for the g-C_3N_4/$Sr_2KNb_5O_{15}$ nanocomposites with low g-C_3N_4 content (24CNNb) and the mixed M77CNNb sample. The two different band gaps as estimated from the Tauc plots can be assigned to the absorption bands of their components. Along with increasing g-C_3N_4 content the intense absorbance of the $Sr_2KNb_5O_{15}$ component disappeared in the UV region and their absorption edges become almost similar to that of bare g-C_3N_4, implying the $Sr_2KNb_5O_{15}$ nanorods were sufficiently covered by a thick g-C_3N_4 layer.

Surface analysis

The X-ray photoelectron spectroscopy (XPS) was employed to analyze the oxidation state and the chemical environment of constituent elements on the surface of the bare $Sr_2KNb_5O_{15}$, 24CNNb and 77CNNb samples. As can be seen from the survey spectra in Fig. 4a, the main constituent elements on the surface of bare $Sr_2KNb_5O_{15}$ sample are Sr, K, Nb, O with sharp photoelectron peaks and low amount of adsorbed C in the form of carbonates. Compared with the XPS spectrum of bare $Sr_2KNb_5O_{15}$, there are no significant changes in binding energy of these constituent elements in the XPS spectra of 24CNNb and 77CNNb nanocomposites (see Fig. S4†). However, the observed content of Sr, K, Nb and O elements significantly decrease while at the same time, the signals of C 1s and N 1s are obviously

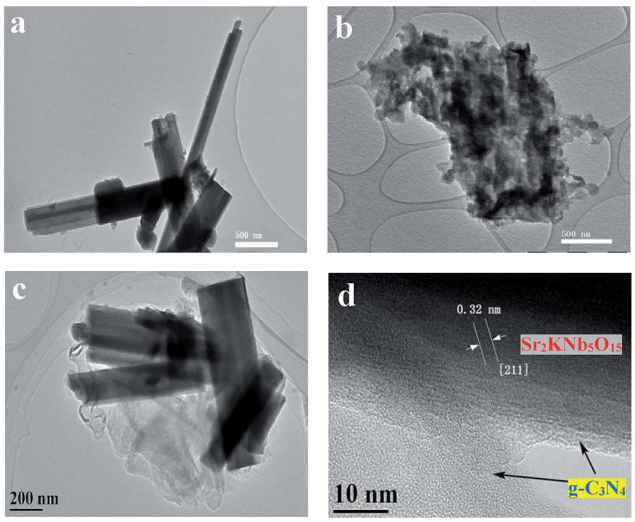

Fig. 2 Representative TEM images of bare $Sr_2KNb_5O_{15}$ (a) bare g-C_3N_4 (b) 77CNNb nanocomposite (c), and HRTEM image of the 77CNNb nanocomposite (d), respectively.

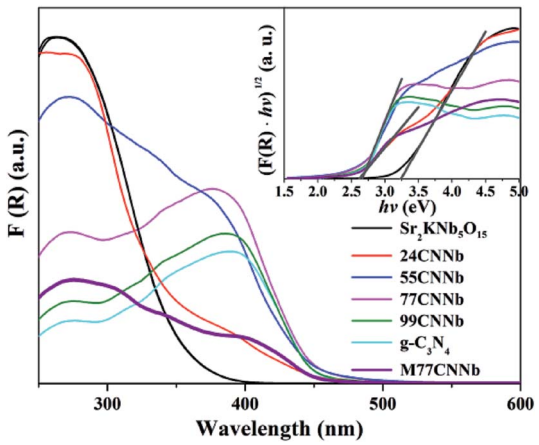

Fig. 3 Kubelka–Munk transformed UV-Vis diffuse reflection spectra and Tauc plots (inset) of the g-C_3N_4/$Sr_2KNb_5O_{15}$ nanocomposite samples.

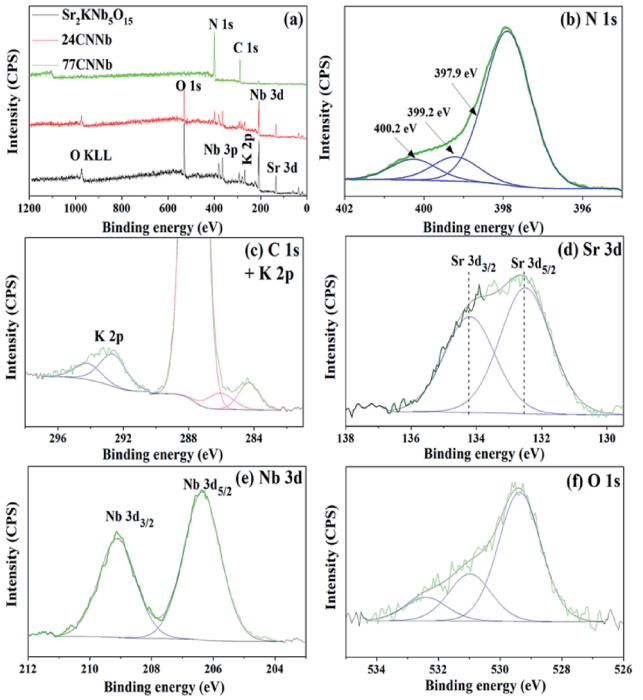

Fig. 4 Survey XPS spectra of bare $Sr_2KNb_5O_{15}$, 24CNNb and 77CNNb nanocomposite samples, respectively (a); and high resolution XPS spectra of N 1s (b), C 1s and K 2p (c), Sr 3d (d), Nb 3d (e) and O 1s (f) of the 77CNNb nanocomposite sample, respectively.

stronger in intensity. As seen in Table 2, with the increasing g-C_3N_4 content from 24CNNb to 77CNNb samples, the calculated atom concentration of N element increases by a factor of about 2.67, in good agreement with the increased amount of g-C_3N_4. However, the atom concentration of Sr and Nb elements decreased by a factor of *ca.* 12.7 and 16.6, respectively, indicating a large amount of g-C_3N_4 covering the surface of $Sr_2KNb_5O_{15}$ nanorods, which is consistent with the TEM observation.

The high resolution N 1s, C 1s, K 2p, Sr 3d, Nb 3d and O 1s XPS spectra of the 77CNNb nanocomposite sample are shown in Fig. 4b–f, respectively. The N 1s XPS spectrum (Fig. 4b) can be deconvoluted into three peaks at 397.9, 399.2, and 400.2 eV, which can be ascribed to C–N–C, N-$(C)_3$ and C–N–H groups of g-C_3N_4.[49,50] The C 1s core level XPS spectrum in Fig. 4c can be fitted into three peaks at 284.3, 286.1 and 287.7 eV, respectively. The XPS peak with binding energy of 284.3 eV can be assigned to the saturated hydrocarbons including adventitious carbon. The peaks at 286.1 and 287.7 eV can be ascribed to the C–N–C and the C–$(N)_3$ group, respectively.[50,51] Therefore, the above results confirm the presence of graphite-like sp^2-bonded graphitic carbon nitride. The XPS spectra of K 2p (Fig. 4c), Sr 3d (Fig. 4d) and Nb 3d (Fig. 4e) can be fitted well into two peaks corresponding to their angular momentum of electron. The K $2p_{3/2}$ and K $2p_{1/2}$ peaks are observed at 292.7 and 294.3 eV, respectively.[52] The Sr $3d_{5/2}$ and Sr $3d_{3/2}$ peaks are located at 132.5 and 134.2 eV, respectively.[53] The Nb 3d peaks at the binding energies of 206.4 and 290.1 eV can be attributed to Nb $3d_{3/2}$ and $3d_{5/2}$ levels, respectively.[54,55] Therefore, the results indicate that only one chemical state for each element of K, Sr, and Nb exists in the nanocomposite, *i.e.*, chemical state of K^+, Sr^{2+}, and Nb^{5+}. Furthermore, Fig. 4f shows that the asymmetric O 1s spectrum can be deconvoluted into three peaks at 529.3, 531.0 and 532.4 eV, respectively. The main peak positioned at a low binding energy of 529.3 eV can be attributed to lattice oxygen in the form of O^{2-}.[56] While the other minor and broad peaks centered at 531.0 and 532.4 eV are usually assigned to the surface adsorbed oxygen in form of CO_3^{2-}, H_2O and O_2.[57–59]

Table 2 Atom concentration (at%) for N, Sr and Nb derived from XPS spectra

Sample	N (at%)	Sr (at%)	Nb (at%)
$Sr_2KNb_5O_{15}$	0	11.97	21.80
24CNNb	19.78	7.77	14.46
77CNNb	52.79	0.61	0.87

Photocatalytic degradation of methylene blue

Fig. S5† shows the wavelength distribution of the irradiation light with a GG400 cutoff filter employed in the photocatalytic degradation of methylene blue (MB) experiments. The photocatalytic abilities of the g-C_3N_4/$Sr_2KNb_5O_{15}$ nanocomposites are presented in Fig. 5a. It is noted that the adsorption of MB on the as-synthesized photocatalysts was negligible after the adsorption–desorption equilibrium was reached in the dark. After irradiation for 6 h, the bare $Sr_2KNb_5O_{15}$ nanorods exhibit almost no activity, due to their relatively large band gap of 3.21 eV, which is only capable of absorbing shortwave ultraviolet light. Meanwhile, it also reflects that the self-sensitized degradation of MB over $Sr_2KNb_5O_{15}$ did not exist in the system and the self-decomposition of MB can be also regarded as negligible. Only 16.2% MB was photodegraded over bare g-C_3N_4 under the same conditions, showing the poor activity of g-C_3N_4. By coupling of g-C_3N_4 with $Sr_2KNb_5O_{15}$, the photocatalytic activities were significantly improved and reached the maximum in the 77CNNb sample and then decreased in 99CNNb sample. The results indicate the cooperative effect between the C_3N_4 and $Sr_2KNb_5O_{15}$ components. The relatively high g-C_3N_4 content in the nanocomposites is very essential to ensure sufficient surface coverage of the $Sr_2KNb_5O_{15}$ nanorods, which presumably plays a crucial role in formation of proper nano-interfaces, thereby leading to the significant improvement of the photocatalytic abilities. Fig. 5b illustrates the variations in characteristic absorbance band of MB at 665 nm, which was assigned to the absorption of the conjugated π-system.[60] It can be clearly seen that the absorbance of MB obviously decreased with the increasing irradiation time over the 77CNNb nanocomposite.

In order to determine the photocatalytic reaction rate, first-order kinetics was confirmed by plotting $\ln(C_0/C)$ against the illumination time. The kinetic equation can be expressed as follows:

$$\ln\frac{C_0}{C} = kt \quad (1)$$

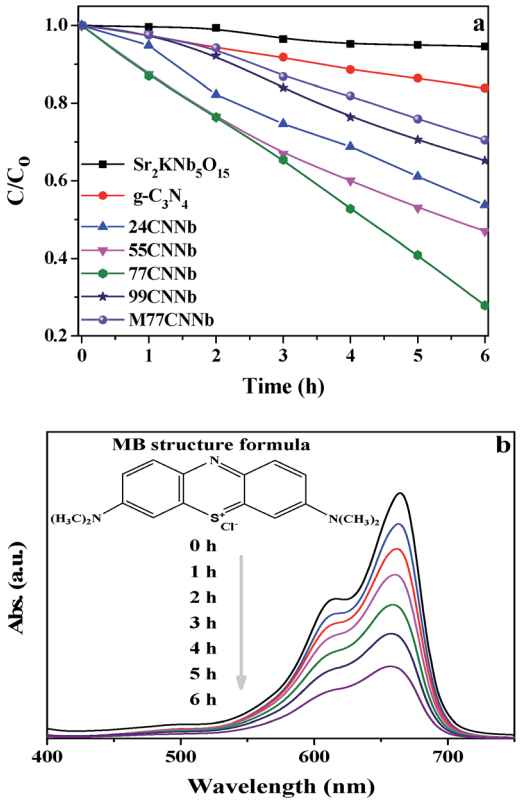

Fig. 5 (a) Photodegradation of MB under visible light (λ > 400 nm) irradiation over g-C_3N_4/$Sr_2KNb_5O_{15}$ nanocomposite samples. The M77CNNb nanocomposite, bare $Sr_2KNb_5O_{15}$ and g-C_3N_4 were also tested for comparison. (b) Absorption changes of MB solution over the 77CNNb nanocomposite sample during photocatalytic process (inset is the MB structural formula).

where C_0 and C are the concentrations of MB solution at times 0 and t in eqn (1), the rate constant of k (h^{-1}) is equal to the corresponding slope of the fitting line, and t is the illumination time (h). The MB photodegradation on each sample follows the first-order kinetics model, as show in Fig. S6.† The resulting rate constants of g-C_3N_4/$Sr_2KNb_5O_{15}$ nanocomposites of different content of g-C_3N_4, M77CNNb nanocomposite, bare $Sr_2KNb_5O_{15}$ and g-C_3N_4 are illustrated in Fig. 6. The photooxidation rate constants of g-C_3N_4/$Sr_2KNb_5O_{15}$ nanocomposites increased with increasing content of the constituent g-C_3N_4. The highest photooxidation rate constant of 77CNNb nanocomposite was estimated to be *ca.* 0.183 h^{-1}, which was about 6.2 times higher than that of the bare g-C_3N_4 (0.029 h^{-1}) and 3.4 times that of the M77CNNb nanocomposite (0.053 h^{-1}). It is worthy to note that the photooxidation rate constant of 99CNNb (0.067 h^{-1}) is still higher than that of bare g-C_3N_4 and M77CNNb nanocomposite. The results indicate that the g-C_3N_4/$Sr_2KNb_5O_{15}$ nanocomposite prepared by direct grown method was greatly beneficial for the formation of the intimate contact between the g-C_3N_4 and $Sr_2KNb_5O_{15}$, thus contributing to improve the electron transfer *via* proper interfaces. In contrast, an improper weight ratio of g-C_3N_4/$Sr_2KNb_5O_{15}$ leads to the loss of favorable interfaces between g-C_3N_4 and $Sr_2KNb_5O_{15}$.

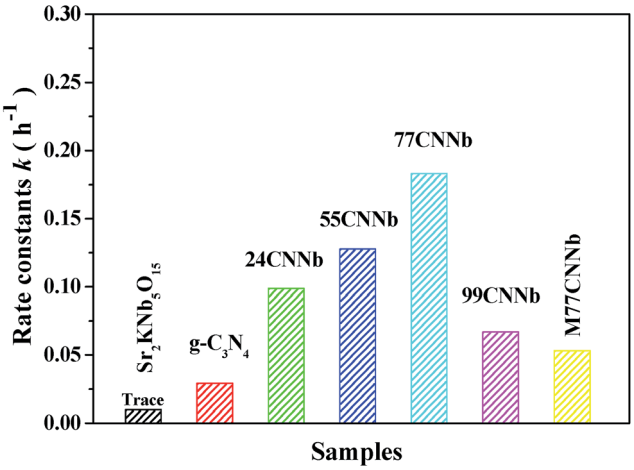

Fig. 6 First-order rate constant for the photodegradation of MB under visible light irradiation (λ > 400 nm) over the g-C_3N_4/$Sr_2KNb_5O_{15}$ nanocomposite photocatalysts with different C_3N_4 content, M77CNNb nanocomposite, bare $Sr_2KNb_5O_{15}$ and g-C_3N_4.

Recyclability

The recyclability of the photocatalyst is an important parameter of the photocatalytic process for practical application. After each cycle, fresh MB solution was used for next photocatalytic experiment, and taking into account the loss of photocatalyst during the sampling process, the photocatalyst was collected from previous parallel experiments followed by washing and drying. As shown in Fig. S7a,† the 77CNNb nanocomposite shows a slight decrease in degradation efficiency after three cycles, which might be due to the trace amount of MB and the degradation byproducts adsorbed on the surface even after intensive washing. As seen from the XRD patterns of the 77CNNb sample before and after the photoreactions (Fig. S7b†), no significant change was observed. Thus it can be concluded that g-C_3N_4/$Sr_2KNb_5O_{15}$ could be recognized as a stable photocatalyst for decomposing organic contaminant pollutants exposed to visible light irradiation.[61–63]

Photoluminescence spectra

Photoluminescence analysis was conducted to understand the electron–hole pair recombination properties of prototypical g-C_3N_4 and 77CNNb nanocomposite samples. As shown in Fig. S8,† the intensity of the broad emission peak appearing at around 440 nm from g-C_3N_4 was obviously higher than that from 77CNNb. The decreased peak intensity in the 77CNNb nanocomposite can be explained by the reduction of the recombination rate of electron–hole pairs, which is consistent with the photocatalytic MB degradation results.

Photocatalytic H_2 production from water splitting

As shown in Fig. 7, under visible light irradiation (λ > 420 nm), the 77CNNb nanocomposite, pristine g-C_3N_4 and $Sr_2KNb_5O_{15}$ samples were further investigated for photocatalytic H_2 production from water splitting. All the measurements were reproducibly conducted at least three times with deviations less

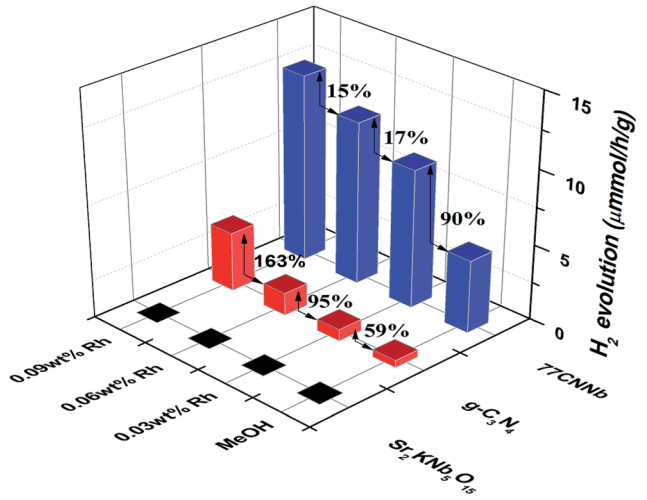

Fig. 7 Time course of photocatalytic H_2 evolution over the 77CNNb nanocomposite, pristine g-C_3N_4 and $Sr_2KNb_5O_{15}$ samples (reaction conditions: catalyst, 30 mg; 30 mL of 10 vol% methanolic solution).

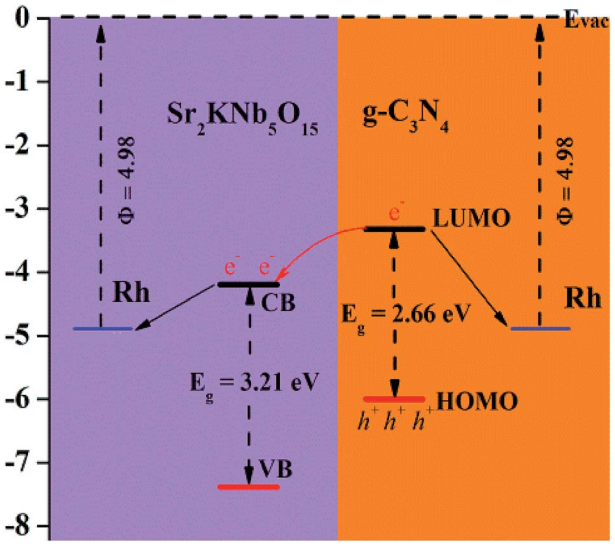

Fig. 8 Proposed mechanism of g-C_3N_4/$Sr_2KNb_5O_{15}$ nanorod nanocomposites.

than 5%. No H_2 evolution was observed for the pristine $Sr_2KNb_5O_{15}$. The presence of methanol as an electron donor and then stepwise photodecomposition of Rh metal as cocatalyst significantly improved the average H_2 production rates of both the g-C_3N_4 and the 77CNNb nanocomposite. However, surprisingly, with stepwise photodecomposition of 0.03 wt% Rh cocatalysts, the enhancement of the g-C_3N_4 was obviously larger than for 77CNNb, as indicated by arrows in Fig. 7. BET surface areas and optical band gaps can be easily excluded as the dominant factor because, as mentioned above, the 77CNNb nanocomposite has a larger BET area than g-C_3N_4 and both of them have a similar band gap. Thus this trend can only be ascribed to an inhibition effect of the deposited Rh, and the large potential difference between Rh and g-C_3N_4, which were probably the most influential factors on the changes of enhancement extent (as will be discussed in detail below).

Proposed photocatalytic mechanism

According to the report by Scaife for oxides not containing partly filled d-levels,[64] the following equation can be used to approximately determine the flat band potential:

$$V_{fb}(\mathrm{NHE}) = 2.94 - E_g \quad (2)$$

where V_{fb} and E_g represent a flat band potential and a band gap, respectively. The conduction band (CB) and valance band (VB) edge potentials of $Sr_2KNb_5O_{15}$ were roughly estimated to be about −0.27 and 2.94 V, respectively. Thus under visible light irradiation, the wide band-gap $Sr_2KNb_5O_{15}$ is photoinactive. On the other hand, Wang, *et al.*[28] reported that by density functional theory (DFT) calculations, the LUMO and HOMO energy levels of g-C_3N_4 are estimated at −1.12 and 1.57 V, respectively. As seen in Fig. 8, effective spatial charge separation between g-C_3N_4 and $Sr_2KNb_5O_{15}$ is proposed to account for the enhanced visible-light photocatalytic activity, *i.e.*, the g-C_3N_4 behaves as visible light absorber, and with the aid of smooth nano-interfaces, the cooperative $Sr_2KNb_5O_{15}$ nanorods act as an electron separator, which is capable of adopting photoexcited electrons from g-C_3N_4. The electron transfer process and redistribution behavior of photogenerated holes in the side of g-C_3N_4 and photogenerated electrons in the side of $Sr_2KNb_5O_{15}$ greatly reduce the possibilities of electron–hole pairs recombination and thus enhance the photodegradation rate. Moreover, in order to understand the effect of Rh metal for interfacial charge transfer process during photocatalytic H_2 production reaction, the work function of Rh metal (~4.98 eV) was provided (Fig. 8).[65] As a result of the high work function value of Rh metal, Schottky barriers at the interfaces were formed between Rh metal with g-C_3N_4 and $Sr_2KNb_5O_{15}$, respectively, thus significantly enhancing the electron transfer efficiencies of the g-C_3N_4 and the 77CNNb nanocomposite for photocatalytic H_2 production. In case of the nanocomposite two electron transfer channels from g-C_3N_4 and $Sr_2KNb_5O_{15}$ to Rh, respectively, will be built up. And considering the formed coverage structure of g-C_3N_4/$Sr_2KNb_5O_{15}$ and large potential difference between g-C_3N_4 and Rh metal, it can be reasonably inferred that Rh metal co-catalysts would be photoreduced preferentially on surface active sites of g-C_3N_4, rather than $Sr_2KNb_5O_{15}$. Therefore, with the increased amount of the deposited Rh on g-C_3N_4, a large amount of the Schottky barriers was formed between Rh with g-C_3N_4. Consequently, the electron transfer between $Sr_2KNb_5O_{15}$ with g-C_3N_4 and Rh metal became weaker and was competitively inhibited. That is probably the primary reason why the enhancement extent on H_2 production rate was decreased in 77CNNb nanocomposite. Note, the study also points out that in the composite materials system the proper use of noble metal as co-catalysts is an important issue for improving photocatalytic performance.

4. Conclusions

In summary, a novel g-C_3N_4/$Sr_2KNb_5O_{15}$ nanocomposite photocatalyst was simply prepared by directly grown graphitic C_3N_4

on $Sr_2KNb_5O_{15}$ nanorods at 520 °C for 4 h. The structure properties, surface morphology and element chemical states of the as-synthesized samples have been investigated. Compared to bare $Sr_2KNb_5O_{15}$, and g-C_3N_4, the photocatalytic property was significantly enhanced by coupling of g-C_3N_4 with $Sr_2KNb_5O_{15}$ for degradation of methylene blue (MB) and photocatalytic H_2 production from aqueous methanolic solution with stepwise *in situ* photodepositon of Rh. The results demonstrated that g-C_3N_4 acts as a visible-light-harvesting unit, and the inner $Sr_2KNb_5O_{15}$ nanorods is capable of adopting photoexcited electrons from g-C_3N_4, thus greatly enhancing spatial charge separation *via* the formed nano-interfaces.

By a comparative investigation of the direct growth method with physical mixing method of pre-synthesized g-C_3N_4 and $Sr_2KNb_5O_{15}$, the photodegradation rate of the former is found to be about 3.4 times higher than of the latter, indicating how important the formation of proper nano-interfaces is. The work may provide further insight for rational construction of C_3N_4-based composite and offer an alternative strategy to develop visible-light-driven photocatalysts for the potential applications of water treatment and other environmental remediation.

Conflicts of interest

There are no conflicts to declare.

Acknowledgements

We greatly appreciate Prof. Dr M. Muhler (RUB, Germany) for his support, Dr T. Reinecke (RUB, Germany) for XRD measurements and Dr W. H. Zhang (RUB, Germany) for the TG measurements. This work was financially supported by the National Natural Science Foundation of China (Grant Number: 51402193, 51572173, 51602197 and 11402149), Shanghai Eastern Scholar Program (Grant Number: QD2016014) and Shanghai Pujiang Talent Program (Grant Number: 16PJ1407700).

Notes and references

1 A. Mills and S. LeHunte, *J. Photochem. Photobiol., A*, 1997, **108**, 1–35.
2 S. K. Lee and A. Mills, *Platinum Met. Rev.*, 2003, **47**, 61–72.
3 F. Wang, T. A. Shifa, X. Zhan, Y. Huang, K. Liu, Z. Cheng, C. Jiang and J. He, *Nanoscale*, 2015, **7**, 19764–19788.
4 F. E. Osterloh, *Chem. Mater.*, 2008, **20**, 35–54.
5 X. B. Chen, S. H. Shen, L. J. Guo and S. S. Mao, *Chem. Rev.*, 2010, **110**, 6503–6570.
6 H. Yamashita, M. Harada, J. Misaka, M. Takeuchi, K. Ikeue and M. Anpo, *J. Photochem. Photobiol., A*, 2002, **148**, 257–261.
7 N. Negishi, M. Fujino, H. Yamashita, M. A. Fox and M. Anpo, *Langmuir*, 1994, **10**, 1772–1776.
8 W. Y. Choi, A. Termin and M. R. Hoffmann, *Angew. Chem., Int. Ed. Engl.*, 1994, **33**, 1091–1092.
9 S. Sakthivel and H. Kisch, *Angew. Chem., Int. Ed.*, 2003, **42**, 4908–4911.
10 R. Asahi, T. Morikawa, T. Ohwaki, K. Aoki and Y. Taga, *Science*, 2001, **293**, 269–271.
11 T. Umebayashi, T. Yamaki, H. Itoh and K. Asai, *Appl. Phys. Lett.*, 2002, **81**, 454.
12 X. Zong, C. H. Sun, Z. G. Chen, A. Mukherji, H. Wu, J. Zou, S. C. Smith, G. Q. Lu and L. Z. Wang, *Chem. Commun.*, 2011, **47**, 6293–6295.
13 R. Marschall and L. Wang, *Catal. Today*, 2014, **225**, 111–135.
14 X. Xu, G. Liu, C. Randorn and J. T. S. Irvine, *Int. J. Hydrogen Energy*, 2011, **36**, 13501–13507.
15 J. Zhang, X. Chen, K. Takanabe, K. Maeda, K. Domen, J. D. Epping, X. Fu, M. Antonietti and X. Wang, *Angew. Chem., Int. Ed.*, 2010, **49**, 441–444.
16 A. Hagfeldt, G. Boschloo, L. C. Sun, L. Kloo and H. Pettersson, *Chem. Rev.*, 2010, **110**, 6595–6663.
17 U. B. Cappel, S. M. Feldt, J. Schoneboom, A. Hagfeldt and G. Boschloo, *J. Am. Chem. Soc.*, 2010, **132**, 9096–9101.
18 P. Wang, P. Chen, A. Kostka, R. Marschall and M. Wark, *Chem. Mater.*, 2013, **25**, 4739–4745.
19 R. Marschall, *Adv. Funct. Mater.*, 2014, **24**, 2421–2440.
20 Z. Cheng, F. Wang, T. A. Shifa, K. Liu, Y. Huang, Q. Liu, C. Jiang and J. He, *Appl. Phys. Lett.*, 2016, **109**, 053905.
21 K. Vinodgopal, I. Bedja and P. V. Kamat, *Chem. Mater.*, 1996, **8**, 2180–2187.
22 Y. Bessekhouad, D. Robert and J.-V. Weber, *Catal. Today*, 2005, **101**, 315–321.
23 Z. Bian, J. Zhu, S. Wang, Y. Cao, X. Qian and H. Li, *J. Phys. Chem.*, 2008, **112**, 6258–6262.
24 K. Li, B. Chai, T. Y. Peng, J. Mao and L. Zan, *ACS Catal.*, 2013, **3**, 170–177.
25 Q. J. Xiang, J. G. Yu and M. Jaroniec, *J. Am. Chem. Soc.*, 2012, **134**, 6575–6578.
26 H. J. Yan and H. X. Yang, *J. Alloys Compd.*, 2011, **509**, L26–L29.
27 P. A. Sant and P. V. Kamat, *Phys. Chem. Chem. Phys.*, 2002, **4**, 198–203.
28 X. Wang, K. Maeda, A. Thomas, K. Takanabe, G. Xin, J. M. Carlsson, K. Domen and M. Antonietti, *Nat. Mater.*, 2009, **8**, 76–80.
29 X. C. Wang, K. Maeda, X. F. Chen, K. Takanabe, K. Domen, Y. D. Hou, X. Z. Fu and M. Antonietti, *J. Am. Chem. Soc.*, 2009, **131**, 1680–1681.
30 Y. Wu and M. Wark, *New Concepts in Photocatalysis*, RSC Publishing, London, 2016, ch. 6, pp. 129–161.
31 N. Yang, G. Q. Li, W. L. Wang, X. L. Yang and W. F. Zhang, *J. Phys. Chem. Solids*, 2011, **72**, 1319–1324.
32 Q. Y. Li, B. Yue, H. Iwai, T. Kako and J. H. Ye, *J. Phys. Chem. C*, 2010, **114**, 4100–4105.
33 Y. Liu, G. Chen, C. Zhou, Y. D. Hu, D. G. Fu, J. Liu and Q. Wang, *J. Hazard. Mater.*, 2011, **190**, 75–80.
34 S. C. Yan, S. B. Lv, Z. S. Li and Z. G. Zou, *Dalton Trans.*, 2010, **39**, 1488–1491.
35 C. Pan, J. Xu, Y. Wang, D. Li and Y. Zhu, *Adv. Funct. Mater.*, 2012, **22**, 1518–1524.
36 L. Ge, C. C. Han and J. Liu, *Appl. Catal., B*, 2011, **108**, 100–107.

37 X. She, J. Wu, H. Xu, J. Zhong, Y. Wang, Y. Song, K. Nie, Y. Liu, Y. Yang and M. T. F. Rodrigues, *Adv. Energy Mater.*, 2017, 1700025.
38 J. Fu, Y. L. Tian, B. B. Chang, F. N. Xi and X. P. Dong, *J. Mater. Chem.*, 2012, **22**, 21159–21166.
39 D. Jiang, L. Chen, J. Zhu, M. Chen, W. Shi and J. Xie, *Dalton Trans.*, 2013, **42**, 15726–15734.
40 B. Chai, T. Peng, J. Mao, K. Li and L. Zan, *Phys. Chem. Chem. Phys.*, 2012, **14**, 16745–16752.
41 Q. Y. Li, L. L. Zong, Y. Y. Xing, X. D. Wang, L. G. Yu and J. J. Yang, *Sci. Adv. Mater.*, 2013, **5**, 1316–1322.
42 H. J. Yan and H. X. Yang, *J. Alloys Compd.*, 2011, **509**, 26–29.
43 J. X. Sun, Y. P. Yuan, L. G. Qiu, X. Jiang, A. J. Xie, Y. H. Shen and J. F. Zhu, *Dalton Trans.*, 2012, **41**, 6756–6763.
44 Y. Zeng, Y. Wang, J. Chen, Y. Jiang, M. Kiani, B. Li and R. Wang, *Ceram. Int.*, 2016, **42**, 12297–12305.
45 L. Sun, Y. Qi, C. J. Jia, Z. Jin and W. Fan, *Nanoscale*, 2014, **6**, 2649–2659.
46 P. Wang, L. Schwertmann, R. Marschall and M. Wark, *J. Mater. Chem. A*, 2014, **2**, 8815–8822.
47 S. C. Yan, Z. S. Li and Z. G. Zou, *Langmuir*, 2009, **25**, 10397–10401.
48 M. Xiong, L. Chen, Q. Yuan, J. He, S. L. Luo, C. T. Au and S. F. Yin, *Carbon*, 2015, **86**, 217–224.
49 G. Zhang, J. Zhang, M. Zhang and X. Wang, *J. Mater. Chem.*, 2012, **22**, 8083.
50 B. Chai, T. Peng, J. Mao, K. Li and L. Zan, *Phys. Chem. Chem. Phys.*, 2012, **14**, 16745–16752.
51 M. Kaba, N. Raklaoui, M. F. Guimon and A. Mas, *J. Appl. Polym. Sci.*, 2005, **97**, 2088–2096.
52 H. Konno, K. Sasaki, M. Tsunekawa, T. Takamori and R. Furuichi, *Jpn. Anal.*, 1991, **40**, 609–616.
53 S. Koba, R. Nagata, M. Onishi, Y. Ozono, K. Shibata, S. Higo, I. Kawano, T. Kushida, Y. Kim and T. Ogushi, *Int. J. Mod. Phys. B*, 1998, **12**, 1755–1762.
54 F. Garbassi, J. Bart and G. Petrini, *J. Electron Spectrosc. Relat. Phenom.*, 1981, **22**, 95–107.
55 T. Xia, Q. Li, J. Meng and X. Cao, *Mater. Chem. Phys.*, 2008, **111**, 335–340.
56 J.-C. Dupin, D. Gonbeau, P. Vinatier and A. Levasseur, *Phys. Chem. Chem. Phys.*, 2000, **2**, 1319–1324.
57 R. Cole, N. Brooks and P. Weightman, *Phys. Rev. Lett.*, 1997, **78**, 3777.
58 N. Wakiya, K. Kuroyanagi, Y. Xuan, K. Shinozaki and N. Mizutani, *Thin Solid Films*, 2000, **372**, 156–162.
59 Y. Zhang-Steenwinkel, J. Beckers and A. Bliek, *Appl. Catal., A*, 2002, **235**, 79–92.
60 P. Qu, J. C. Zhao, T. Shen and H. Hidaka, *J. Mol. Catal. A: Chem.*, 1998, **129**, 257–268.
61 H. Cheng, B. Huang, Y. Dai, X. Qin and X. Zhang, *Langmuir*, 2010, **26**, 6618–6624.
62 S. Y. Chai, Y. J. Kim, M. H. Jung, A. K. Chakraborty, D. Jung and W. I. Lee, *J. Catal.*, 2009, **262**, 144–149.
63 Y. Zang and R. Farnood, *Appl. Catal., B*, 2008, **79**, 334–340.
64 D. E. Scaife, *Sol. Energy*, 1980, **25**, 41–54.
65 W. M. Haynes, *CRC handbook of chemistry and physics CD-ROM version*, 90th edn, 2010.